Slab tearing in non-collisional settings: Insights from thermo-mechanical modelling of oblique subduction

Nevena Andrić-Tomašević [a,b,*], Alexander Koptev [b,c], Giridas Maiti [a], Taras Gerya [d], Todd A. Ehlers [b]

[a] Institute of Applied Geosciences, Karlsruhe Institute of Technology, Germany
[b] Department of Geosciences, University of Tübingen, Germany
[c] GFZ German Research Centre for Geosciences, Potsdam, Germany
[d] Institute of Geophysics, ETH Zurich, Switzerland

A B S T R A C T

The propagation of slab break-off (slab tearing) is usually attributed to laterally variable plate convergence systems with a spatial transition between simultaneous oceanic subduction and continental collision. To study the process of slab tearing in a non-collisional geodynamic context, here we use a 3D thermo-mechanical numerical approach to model the oblique subduction of a homogeneous oceanic plate. We investigate the effects of the following parameters: (1) subduction obliquity angle, (2) age of oceanic slab, and (3) partitioning of boundary velocities (i.e., the ratio between the subduction component and the advance of the overriding plate in the total convergence). In our simulations, the retreat of the subduction zone leads to a thinning of the fore-arc and back-arc lithosphere, which are decoupled from the subducting slab by the rise of the hot asthenosphere from the underlying mantle wedge. As a consequence of the initial obliquity of the active plate margin, slab roll-back velocities are subject to progressive along-trench variations. Consistent with the gradual rotation of the trench, the front of the decoupling between the overriding and downgoing plates (together with predicted magmatic activity and topographic uplift) migrates in a horizontal direction. In the experiments with low angles of subduction obliquity (< 15°), relatively old subducting plates (> 50 Ma), and in the absence of the subduction component in the overall shortening, slab detachment either develops simultaneously along the entire length of the subduction zone or does not occur at all. In contrast, with higher subduction obliquity ($\geq$ 15°), younger slabs ($\leq$ 50 Ma) and in the presence of a boundary push on the oceanic side, the initial slab break-off is followed by the gradual growth of the "tear" window in the direction opposite to the migration path of the previously established plates decoupling. The sharp contrast in trench retreat rates between subduction zone segments affected and unaffected by slab detachment results in the arcuate shape of the trench. Furthermore, the direction of slab tearing may change from horizontal to vertical, eventually leading to the formation of a transform fault on the subducting plate. Our results show striking similarities with several features – such as trench curvature, subduction zone segmentation, magmatic production, lithospheric stress/deformation fields, and associated topographic changes – observed in many subduction zones (e.g., Marianas, New Hebrides, Mexico, Calabrian).

1. Introduction

Slab break-off (also termed slab detachment) is the geodynamic process by which the lower part of a subducted slab separates from its upper part and subsequently sinks into the Earth's mantle. The concept of slab break-off emerged more than half a century ago from the analysis of seismological data as an explanation for gaps in hypocentral distributions between deep and intermediate-depth earthquakes (Isacks and Molnar, 1969; Barazangi et al., 1973). Several decades later, seismic tomography revealed positive velocity anomalies that can be interpreted as detached slab fragments in the upper (Spakman, 1990; Wortel and Spakman, 2000) and lower (Hafkenscheid et al., 2006) mantle. Since the turn of the

millennium, slab break-off has become the subject of numerous 2D modelling studies highlighting various dynamic and kinematic aspects associated with this process (see the review by Gerya, 2011 and references therein). In particular, progressive viscous thinning of the subducting plate has been shown to be a predominant deformation mechanism during slab detachment (Burov and Yamato, 2008; Baumann et al., 2010; Duretz et al., 2012a), occurring at greater depths and with greater time lag as subducting plate age or convergence rates increases (Duretz et al., 2011). Partial or complete loss of slab pull force due to slab break-off results in what is known as "slab eduction": a coherent backward movement of previously subducted rocks (Andersen et al., 1991; Duretz et al., 2012b; Andrić et al., 2018), accompanied by topographic uplift ranging between 6 km (Buiter et al., 2002) to 1-1.5 km (Gerya et al., 2004). The inflow of hot asthenosphere at the site of slab detachment significantly raises the temperature of the overlying material (Van de Zedde and Wortel, 2001), allowing partial melting and associated magmatism (Altunkaynak and Genç, 2008).

Based on a 3D seismic velocity structure of the Mediterranean lithosphere and upper mantle, Wortel and Spakman (1992) formulated the hypothesis of spatial migration of plate detachment (also called "slab tearing") as a new element in the dynamics of the lithosphere. Spatially and temporally progressive surface effects such as the uplift of topography along the Apeninic foredeep (Van der Meulen et al., 1999), migrating foreland basin depocenter along the Alps-Carpathians fold and thrust belt (Meulenkamp et al., 1996) and migrating pulse of mafic volcanism in central Mexico (Ferrari, 2004) are archetypal examples of data-based confirmation of slab break-off as a 3D process expressed by lateral propagation of a horizontal tear. Burkett and Billen (2010) and Van Hunen and Allen (2011) pioneered the first fully-dynamic 3D thermomechanical models for slab tearing. According to these studies, the detachment of a laterally symmetric and homogeneous subducting plate occurs nearly simultaneously along the entire length of the slab. In contrast, lateral heterogeneities of the incoming plate, which include mid-oceanic ridge segments (Burkett and Billen, 2010) or continental blocks (Van Hunen and Allen, 2011), result in horizontally propagating break-off controlled by spatial variations in slab pull along the subduction zone. These outcomes inspired subsequent modelling efforts to explore the dynamics of a continental corner (lateral continental/oceanic transition zone) during simultaneous oceanic subduction and continental collision (Li et al., 2013; Duretz et al., 2014; Sternai et al., 2014; Menant et al., 2016). The main conclusion from these investigations is that slab detachment first initiates beneath the collided continents and then propagates parallel to the trench (Li et al., 2013). Importantly, the propagation of slab break-off (slab tearing) is always accompanied by relatively faster slab roll-back in the domain of continuous subduction than in the locked collisional segment (Sternai et al., 2014; Menant et al., 2016). Similar along-trench variations in slab retreat rates have also been noted in recent modelling studies (Malatesta et al., 2013, 2016; Balázs et al., 2021) that address the process of the oblique subduction (i.e., subduction in which the plate convergence vector and the trench are not perpendicular to each other). In these experiments, the lateral mantle flow gradient induced by the initial obliquity of subduction leads to a gradual rotation of the trench toward a direction more orthogonal to shortening. The associated laterally variable subduction velocities have been shown to control the tectonic transport of sediments along the trench (Malatesta et al., 2013, 2016) and the deformation pattern in the overriding plate (Balázs et al., 2021). Despite the advances of the previous studies, the consequences of the oblique trench geometry for possible slab detachment and/or tearing have not yet been explored, despite being captured by tomographic imaging in numerous subduction zones worldwide: e.g., Izu-Bonin-Marianas (Stern et al., 2004; Miller et al., 2006; Zhang et al., 2019), Tonga (Bevis et al., 1995; Martin, 2014), Mexico (Rogers et al., 2002), and Sunda (Curray, 1989; Widiyantoro and van der Hilst, 1996).

Traditionally, the subduction termination by slab break-off is considered as a consequence of collision between active subduction zones and buoyant continental terranes, mid-oceanic ridges, magmatic arcs, oceanic plateaus, or seamount chains (Gerya, 2011, 2022 and references therein). Here we examine, for the first time, the process of slab detachment and tearing in a non-collisional geodynamic context. To this end, we have performed a series of 3D thermo-mechanical models for the oblique subduction of a homogeneous slab. We demonstrate that for a suitable combination of initial and boundary conditions (such as high angle of subduction obliquity, young age of the subducting plate, and predominant subduction component in the total convergence), an overall rotation of the retreating trench due to the oblique setting is followed by slab break-off that propagates in both the horizontal and vertical directions. Although our experiments are generalized and do not focus on any particular natural case, comparison with observations sheds new light on the characteristic features of different subduction zones.

2. Modelling approach

We investigated the non-collisional process of oblique subduction and associated slab break-off and tearing with numerical experiments performed using the viscous-plastic code I3ELVIS (Gerya and Yuen, 2007; Gerya, 2019). This thermomechanical model is based on coupled conservative finite differences and marker-in-cell methods. The momentum, continuity, and energy equations are solved on the fixed Eulerian grid, whereas the physical properties are transported by Lagrangian markers that follow the velocity field. The model accounts for the major phase transitions in the Earth's mantle as well as adiabatic, radiogenic, and frictional internal heating sources. The viscous material deforms according to dislocation and diffusion creep laws, while the brittle/plastic regime is formulated in terms of the Drucker-Prager failure criterion. The rheological model also includes strain-induced brittle weakening and ductile damage due to grain-size reduction (see Gerya et al., 2021 and Methods in Appendix A for more details).

2.1. Initial model setup

The 3D model box has a size of 2000 × 1500 km in the horizontal and 780 km in the vertical direction. The domain of the 3D model consists of 303 × 237 × 171 nodes, giving a spatial resolution of ∼6.5 × 6.5 × 4.5 km per grid cell. This implies very large mesh sizes (more than ten million elements and a hundred million randomly distributed Lagrange markers) and therefore requires a considerable computation time.

The setup involves a continental overriding plate and a subducting plate built up by an oceanic lithosphere, which are separated by an oblique boundary (Fig. 1). The initial subduction obliquity (i.e., the angle on the map view between the ocean-continent boundary and the lateral borders of the model) is varied from 0° to 22.5° in increments of 7.5° (see section 2.2). The continental lithosphere is composed of a 40 km thick crust, evenly divided into a felsic upper crust (wet quartzite rheology) and a mafic lower crust (plagioclase rheology), and a 50 km thick mantle. Initial nonlinear continental geotherm is computed from a steady-state approximation for a boundary temperature of 0 °C at the surface and an initial temperature of 1300 °C at the lithosphere-asthenosphere boundary (e.g., Artemieva, 2006; Koptev and Ershov, 2011), taking into account radiogenic heat production in the lithospheric layers (for thermal parameters, see Table A.1). The oceanic crust is represented by 3 km of basalts and a 5 km thick gabbroic layer. The thermal structure of the oceanic lithosphere is defined using
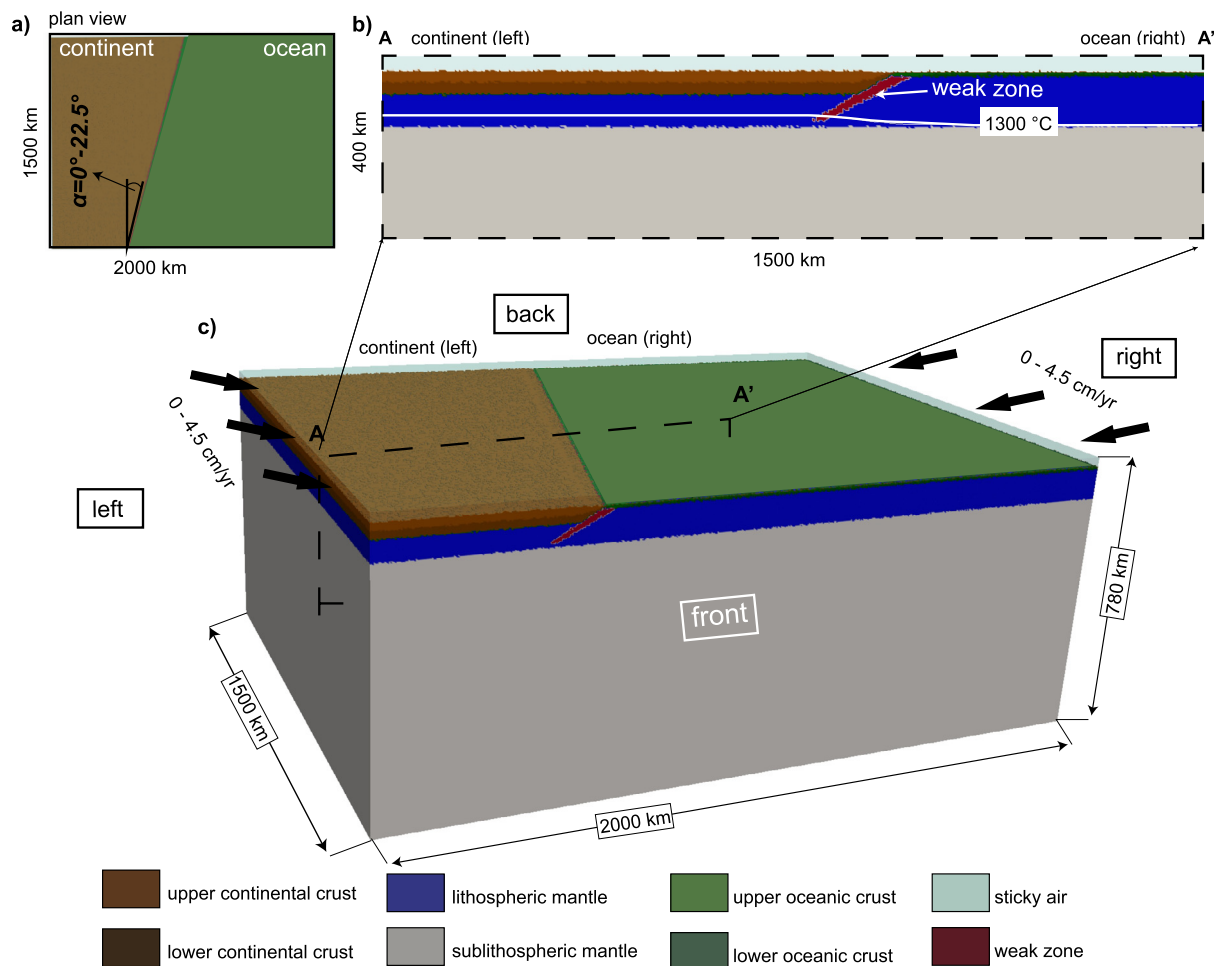
Fig. 1. Design of the 3D model setup: a) map view of the model box showing the oblique geometry of the active plate margin; b) vertical profile across the central part of the model demonstrating the position of the 1300 °C isotherm and the initial weak zone characterized by low plastic strength (see Table A.2), that enables subduction of the incoming oceanic lithosphere beneath the overriding continent (e.g., Koptev et al., 2019); c) 3D view illustrating the velocity boundary conditions on the left and right sides of the model domain.

a half-space cooling age that ranges from 20 to 90 Ma (see section 2.2). Both the lithospheric (oceanic and continental) and the sublithospheric mantle consist of anhydrous peridotite described by the dry olivine flow law (for rheological parameters, see Table A.2). The initial adiabatic temperature gradient in the sublithospheric mantle is ∼0.5 °C/km.

On the right (oceanic) or/and left (continental) side of the model box, we apply kinematic boundary conditions with uniform and time-independent boundary velocities parallel to the long side of the model, mimicking plate driving forces such as ridge push and basal drag (e.g., Bird, 1998). The resulting lateral shortening is therefore accommodated by subduction of the oceanic plate or/and migration (or advance) of the overriding continent. The relation between the boundary velocities applied on the right (subduction component) and left (advance of the overriding plate) sides of the model represents a variable parameter of this study (see section 2.2). The total convergence rate, however, remains the same (4.5 cm yr^{-1}) in all experiments. Free slip is assumed to be the kinematic boundary condition for the front and back sides of the model. The free slip condition requires that the two non-orthogonal components of the velocity do not change across the boundary, while the normal component is zero.

The upper part of the model consists of a 22 km thick layer of "sticky air" with low viscosity (10^{18} Pa s) and low density (1 kg m^{-3}), which allows the top of the crust to be approximated as a free surface (Crameri et al., 2012). To ensure mass conservation

within the model domain, constant outflows are imposed at the top and bottom boundaries, compensating for the net product of the applied horizontal shortening under the Eulerian configuration framework.

2.2. Modelling procedure

The three main parameters of our study are (1) the angle of the subduction obliquity, (2) the age of the subducting slab, and (3) the partitioning of the boundary velocities (Table 1). We begin with a reference experiment (model **1**) characterized by a subduction obliquity angle of 15°, an oceanic plate age of 30 Ma, and a boundary push of 4.5 cm yr^{-1} from the right (oceanic) side of the model. We then test the subduction obliquity changing from 0° (model **2**) through 7.5° (model **3**) to 22.5° (model **4**), and the thermal age of the subducting oceanic lithosphere ranging from 20 to 90 Ma (models **5-9**). Subsequently, we examine a different partitioning of the velocity boundary conditions: in model **10**, the total convergence velocity of 4.5 cm yr^{-1} was achieved by half-rates (2.25 cm yr^{-1}) on both the right (oceanic) and left (continental) sides, whereas in model **11**, the boundary velocity of the same value (4.5 cm yr^{-1}) but of the opposite direction is applied only on the left (continental) side of the model box. Finally, three additional experiments (see Table 1) are conducted to test the role of rheological weakening mechanisms (model **12**), the type of the overriding plate (model **13**), and the lateral extent of horizontal di-

Table 1
Controlling parameters of the numerical experiments.

No.	Model parameters			
	Angle of subduction obliquity [°]	Age of subducting slab [Ma]	Boundary velocity [cm yr^{-1}]	
			Left (continental) side	Right (oceanic) side
1 (reference model)	15	30	0	4.5
2	**0**	30	0	4.5
3	**7.5**	30	0	4.5
4	**22.5**	30	0	4.5
5	15	**20**	0	4.5
6	15	**40**	0	4.5
7	15	**50**	0	4.5
8	15	**60**	0	4.5
9	15	**90**	0	4.5
10	15	30	**2.25**	**2.25**
11	15	30	**4.5**	**0**

Three additional experiments: 1) model **12**: reference configuration (as in model **1**) without brittle and ductile weakening; 2) model **13**: ocean-ocean subduction (60 Ma slab as in model **8** subducting beneath 30 Ma overriding oceanic plate); 3) model **14**: high obliquity configuration (as in model **4**) with an oceanic (right) domain extended by 330 km.

mension to evaluate the possible boundary effect for the case of a high subduction obliquity (model **14**).

3. Results

3.1. Reference model

In the reference model **1** (subduction obliquity of 15°, slab age of 30 Ma, boundary push from the oceanic side; Figs. 2–4), the oceanic plate begins to subduct along the prescribed oblique zone of weakness into the mantle beneath the continent (Fig. 2a), forming a narrow and steep trench in the surface topography (Fig. 3a-b). The obliquity of the vector of plate convergence with respect to the ocean-continent boundary results in a dextral strike-slip component in the deformation field along the active margin (Fig. 4a1).

After ~6.5 Myr of model evolution, the subducting plate begins to retreat (Fig. 2b), while the continental lithosphere of the overriding plate is replaced by hot asthenospheric material rising from the mantle wedge (Fig. 4b2). Despite the identical thermal age and initial length of the subducting slab along the trench, the process of subduction roll-back and associated decoupling between the overriding and downgoing plates develops asymmetrically due to the lateral gradient in mantle return flow (see Balázs et al., 2021) and momentum forces (see Lallemand et al., 2008; Li and Gurnis, 2023) caused by the obliquity of the active margin. As a consequence, the decoupling of plates occurs at the frontal side of the model (Fig. 2b), where the velocity of trench retreat is highest. Along-trench variations of slab retreat rates promote a gradual rotation of the subduction zone, accompanied by progressive decoupling, whose front migrates horizontally toward the back of the model domain and also oceanward following slab roll-back (Fig. 2c). This process is reflected in the surface uplift (Fig. 3c-d) and extensional deformation (Fig. 4b1) in the thinned fore-arc and back-arc lithosphere, which is underlain by the uplifted asthenosphere. As decoupling progresses, the width of the near-trench area where the surface is uplifted increases, reaching ~400 km at 9.2 Myr at the front of the model (Fig. 3e).

Hot asthenospheric material at the shallow levels beneath the overriding plate (~40 km depth; Fig. 2d) provides favourable temperature (~1200 °C) and pressure (0.5-1 GPa) conditions for partial melting (Katz et al., 2003) not only in the mantle wedge but also in the crust of the subducting slab, giving rise to boninitic and adakitic magmas (e.g., Ribeiro et al., 2013). The front of partial melting migrates consistently with the propagation of decoupling (Fig. 2d), while the expected amount of total melt increases over time as the decoupling zone expands (Fig. S1). Furthermore, the

upwelling of the asthenosphere leads to an increase in the heat flow up to ~140 mW m^{-2}.

When the decoupling of plates reaches the back side of the model domain at ~9 Myr, the progressive rotation of the trench terminates in a nearly convergence-perpendicular alignment of the active margin. Simultaneously, the subducting lithosphere undergoes necking followed by slab break-off caused by the combined effects of variations in dynamic pressure along the trench (Balázs et al., 2021) and the implemented rheological weakening mechanisms (Gerya et al., 2021). The initial detachment of the slab occurs on the back of the model at a relatively shallow (~120 km) depth (Fig. 2e). The location of break-off initiation is determined by the maximum steepness of the slab (and hence the maximum vertical component of the slab pull force) on the backside edge, which is characterized by a minimal effect of plates decoupling compared to the central and front segments, where active uplift of the hot asthenosphere in the mantle wedge makes the shallow part of the slab less steep.

The initial slab break-off transitions into a self-sustaining horizontal tearing toward the opposite (frontal) boundary of the model box (Fig. 2f). This process is accompanied by toroidal mantle flow around the newly formed slab edge (Fig. 4c2) and corresponding toroidal-like deformation at the crustal level (Fig. 4c1). The continuous and long slab in the central and frontal part of the model retreats much faster than the back segment, where the newly established subduction zone initiated after slab break-off remains quasi-stable because the pull of the relatively short new slab is almost completely compensated by the applied plate convergence. Such an abrupt lateral change in the roll-back rates leads to a highly arcuate trench geometry (Fig. 3f-g).

Subsequently, the horizontal tear begins to propagate in a vertical direction, following the bend of the trench (Fig. 2g). As a result, the slab remains unbroken in its deepest part, but progressively tears at the shallower levels, first horizontally and then vertically (Fig. 2h). In the last phase, vertical tearing evolves into the transform fault (Fig. 3h), offsetting two independent segments of the subduction zone (Fig. 2g).

### 3.2. Effect of subduction obliquity

In addition to the reference experiment characterized by a subduction obliquity of 15° (model **1**; Fig. 2), variable obliquity angles of 0°, 7.5°, and 22.5° (models **2**-**4**) were tested (Fig. S2-S4). In the case of the convergence-perpendicular active margin (obliquity angle of 0°, model **2**), the rate of slab retreat is constant along the trench, and therefore decoupling of plates begins simultaneously
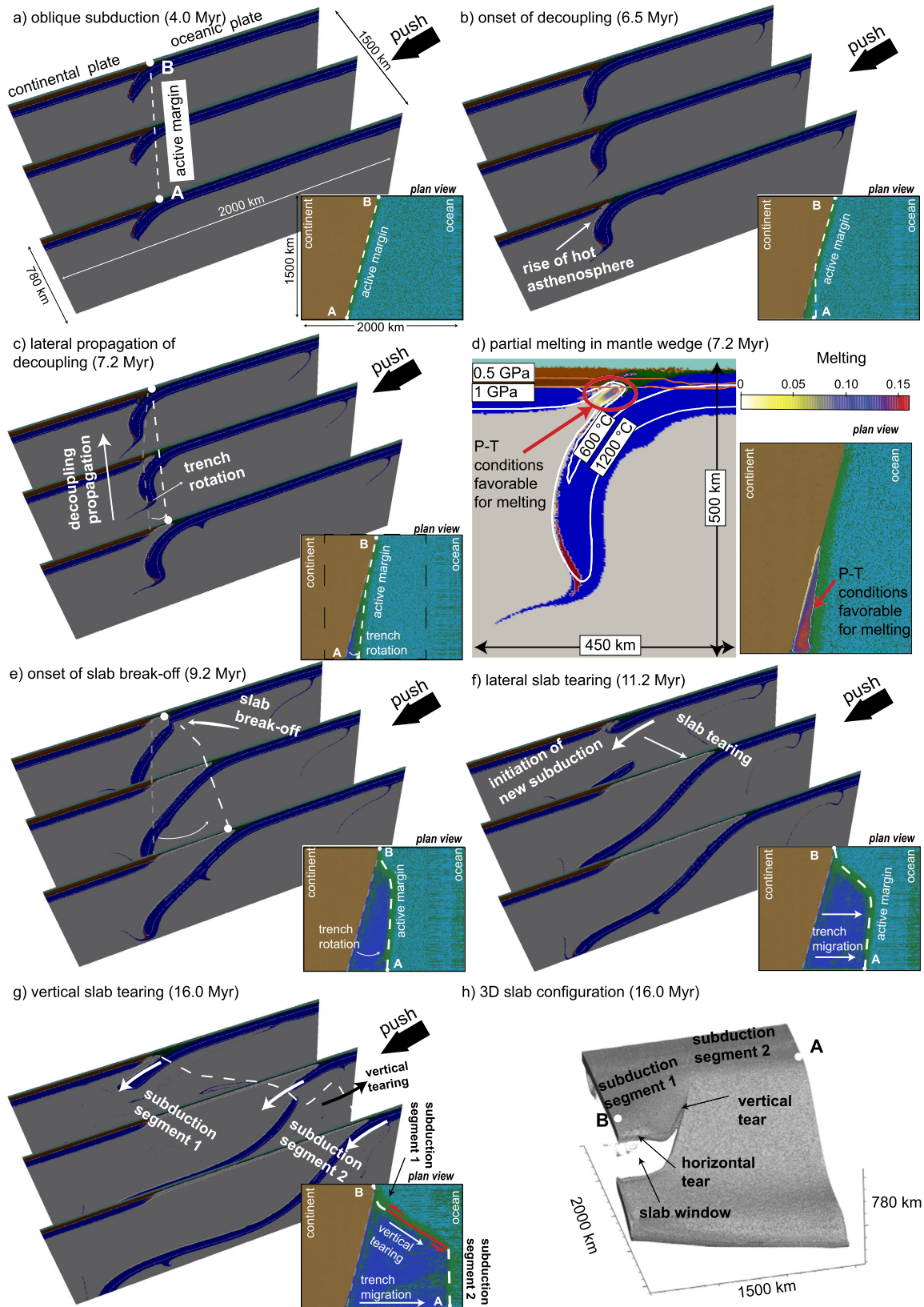
Fig. 2. Compositional field evolution of reference model **1**: a) oblique ocean-continent subduction (4.0 Myr); b) onset of decoupling between the overriding and subducting plates on the frontal side of the model domain (6.5 Myr); c) lateral propagation of decoupling accompanied by counterclockwise trench rotation (7.2 Myr); d) partial melting in the mantle wedge (7.2 Myr) evaluated as a function of modelled P-T conditions for melt parametrization by Katz et al. (2003); e) onset of slab break-off on the back side of the model domain (9.2 Myr); f) lateral slab tearing toward the opposite (frontal) side (11.2 Myr); g) transition from horizontal to vertical slab tearing and formation of the transform fault (16.0 Myr); h) 3D configuration of the subducting plate showing the slab window resulting from progressive horizontal tear propagation transforming into vertical tearing (16.0 Myr). Compositional plan views correspond to horizontal slices at 5 km depth. The partial melt plan view shown in panel "d" corresponds to a depth of 40 km. Figure conventions as in Fig. 1.
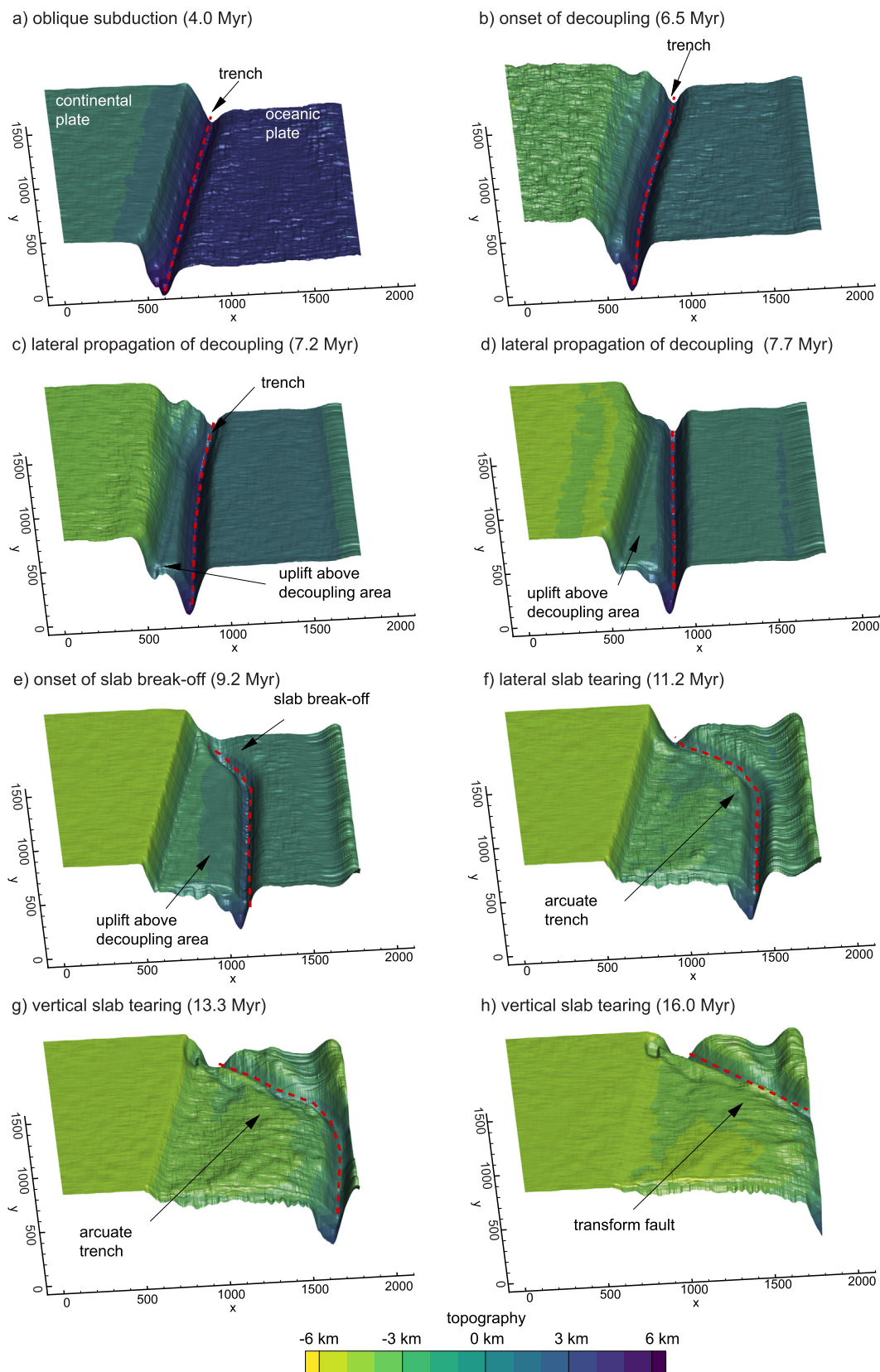
Fig. 3. Surface topography evolution of reference model **1**: a) oblique subduction (4.0 Myr); b) onset of decoupling between the overriding and subducting plates (6.5 Myr); c-d) lateral propagation of decoupling and associated surface uplift in the fore-arc and back-arc area (7.2-7.7 Myr); e) onset of slab break-off (9.2 Myr); f-g) lateral slab tearing and associated bending of the trench (11.2-13.3 Myr); h) vertical slab tearing and transform fault formation (16.0 Myr).
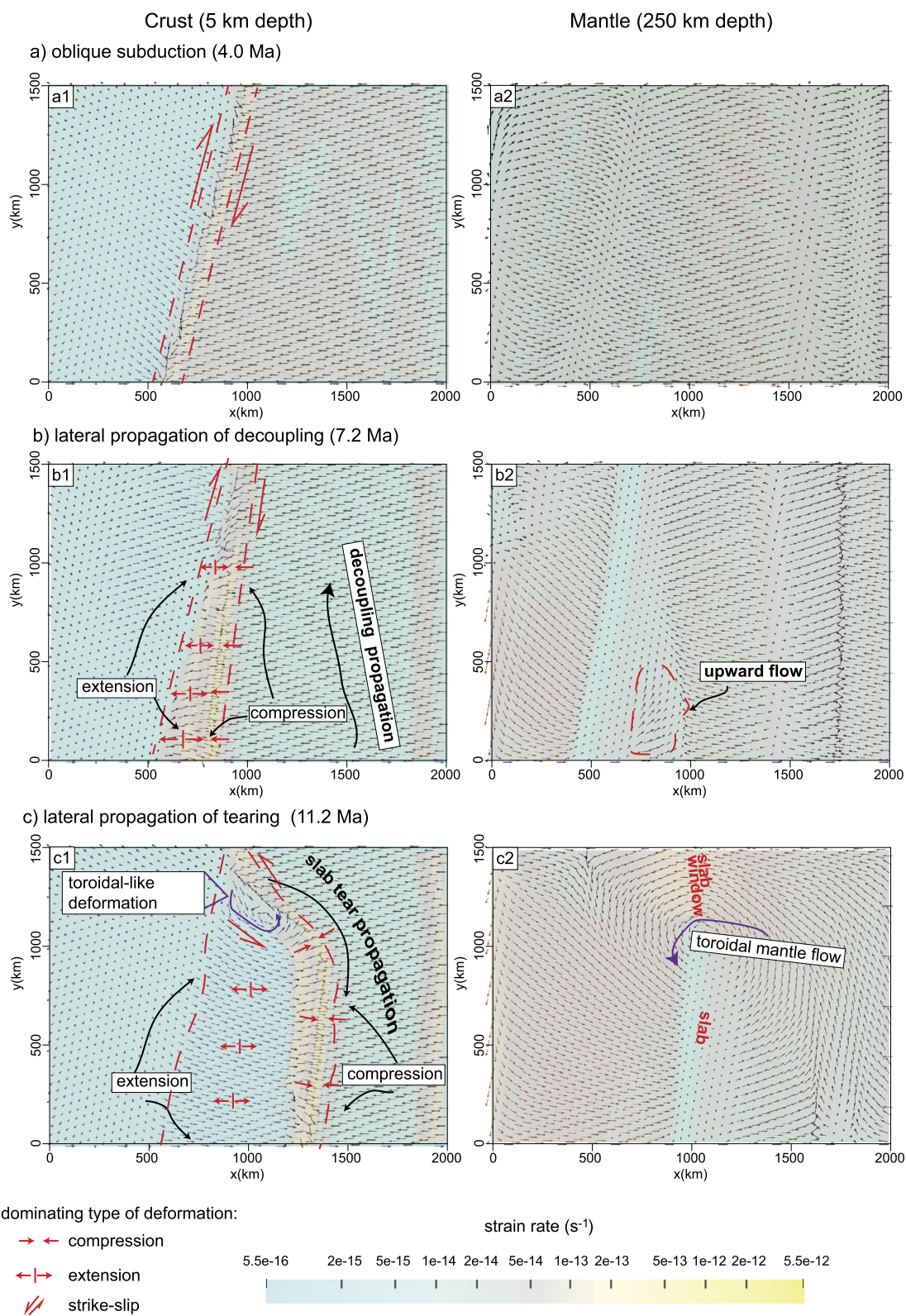
Fig. 4. Strain rate and velocity field evolution of reference model **1** shown for horizontal slices in the crust (depth of 5 km; left column) and mantle (depth of 250 km; right column).
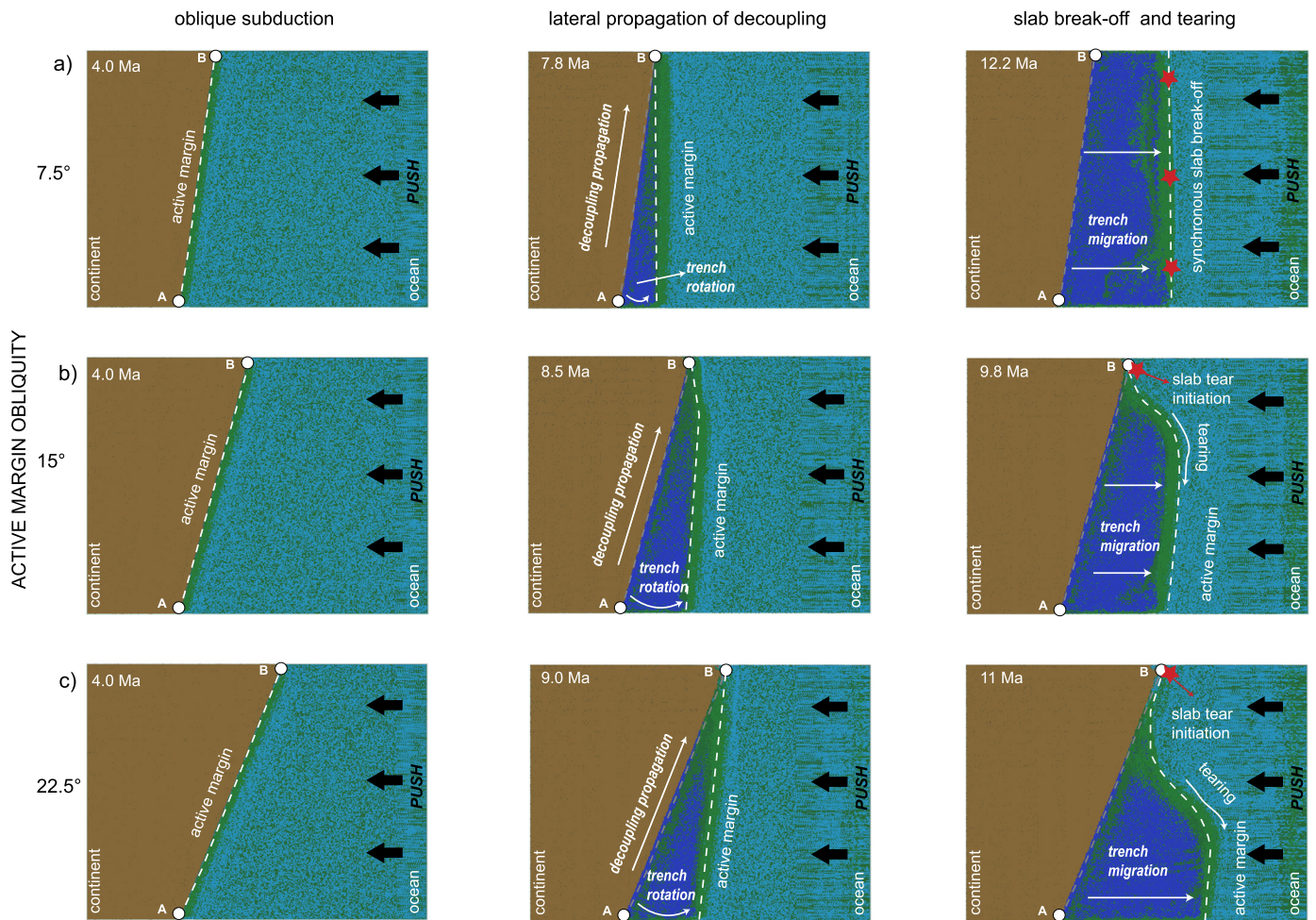
Fig. 5. Plan view of the evolution of the experiments with different obliquity of the active margin: a) model **3** (obliquity angle of 7.5°); b) model **1** (obliquity angle of 15°); c) model **4** (obliquity angle of 22.5°). Figure conventions as in Fig. 1.

along the entire length of the subduction zone. The implementation of obliquity in the model setup results in the propagation of decoupling along the trench, which reaches a rate of ~150 cm yr^{-1} at low obliquity (7.5°; model **3**), whereas it is two times slower (~75 cm yr^{-1}) at reference (15°; model **1**) and high (22.5°; model **4**) obliquity (Fig. 6a).

In model **2**, without an initial oblique component (angle of 0°), slab break-off does not occur, while slab detachment propagates almost instantaneously along the trench when the oblique component is small (7.5°; model **3**). In contrast, a more pronounced obliquity leads to gradual propagation of slab break-off (tearing), which is slower at the reference angle (15°; model **1**) than at a high angle (22.5°; model **4**): the corresponding rates are ~10-15 and ~65 cm yr^{-1}, respectively (Fig. 6b).

Similar to reference model **1** (Fig. 2), high-obliquity model **4** also records a transition from lateral to vertical tearing (Fig. S4), preceded by bending of the trench related to the sharp contrast in slab migration rates between segments of the subduction zone which are affected and unaffected by slab break-off (Fig. 5b-c). On the contrary, the trench remains straight when slab break-off is instantaneous as in low-obliquity model **3** (Fig. 5a).

3.3. Effect of slab age

The main timing characteristics for the decoupling process remain similar for all tested ages of the subducting plate (onset at ~6-7 Myr after the beginning of the experiment and propagation

rate of ~70-80 cm yr^{-1}), except for model **9** with a 90 Ma old slab, where decoupling starts ~2-3 Ma later and propagates faster at a rate of ~120 cm yr^{-1} (Fig. 6a).

For the youngest slab (age of 20 Ma; model **5**), the low rate of horizontal slab tearing (10-15 cm yr^{-1}; Fig. 6b) ensures bending of the trench and subsequent vertical tearing of the slab (Fig. S5), as in the case of the reference age of 30 Ma (model **1**; Fig. 2). For the intermediate ages of subducting plate (40-50 Ma), slab break-off begins ~3 Myr later than in the reference case and propagates extremely rapidly at a rate of ~150 cm yr^{-1} (Fig. 6b), preventing the development of strong trench curvature and the vertical tearing phase (models **6-7**; Fig. S6-S7). For the oldest slabs (60-90 Ma), slab break-off does not occur at all (models **8-9**; Figs. S8-S9).

3.4. Effect of boundary velocities partitioning and additional parameters

The change to an equal partitioning of boundary velocities (i.e., push from both sides, oceanic and continental, as in model **10**) leads to faster (~65 cm yr^{-1}) propagation of slab break-off (Fig. 6b) while the other features such as lateral propagation of decoupling and tearing-induced bending of the trench (Fig. S10), remain the same as in the reference model (Fig. 2). In the absence of the subduction component in the overall convergence, the model with push only from the continental side (model **11**) results in quasi-synchronous break-off along the trench without the development of curvature of the active margin and vertical slab tearing (Fig. S11).
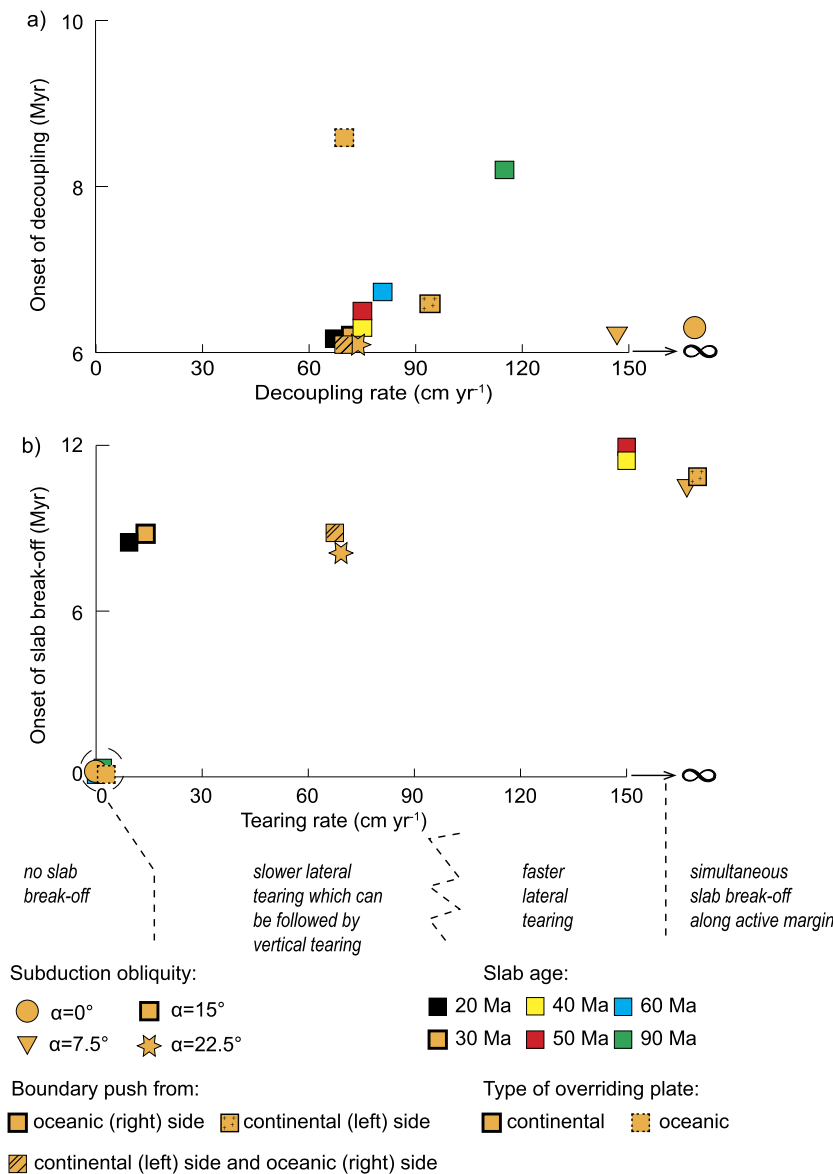
Fig. 6. The key timing characteristics of the models: a) onset of decoupling and decoupling rate; b) onset of slab break-off and tearing rate.

To test the role of the implemented weakening mechanisms (see Gerya et al., 2021 and Methods in Appendix A), we supplement our study with an additional model **12** that excludes the effects of brittle softening and ductile damage. This experiment shows a fundamentally different system behaviour than all other models presented in our study. The absence of rheological weakening hinders the decoupling of plates. As a consequence, the position and orientation of the trench remain unchanged throughout model development, thus precluding retreat and rotation of the trench and subsequent slab break-off (Fig. S12). Consistent with previous studies (Gerya and Meilick, 2011; Baitsch-Ghirardello et al., 2014), this result highlights the importance of implementing weakening mechanisms in subduction modelling.

Another additional model **13** was developed to explore intra-oceanic subduction setting where an oceanic slab subducts beneath the oceanic overriding lithosphere (Fig. S13). This case of ocean-ocean subduction generally exhibits similar behaviour to the corresponding case of ocean-continent subduction (model **8**; Fig. S8), except for the timing of the onset of decoupling, which is delayed by ~2 Myr (Fig. 6a).

Finally, to test the possible effect of a close boundary to the active margin, as in the case of a high subduction obliquity (angle of 22.5°), we performed an experiment with an oceanic (right) domain extended by 330 km (model **14**). This model generally replicates the same evolutionary stages as the corresponding standard-size experiment (model **8**; Fig. S8), except for the final phase of vertical tearing (Fig. S14).

4. Discussion

4.1. Summary of numerical results

In our experiments, the velocity of the downward motion of the subducting plate exceeds the overall convergence rate, resulting in slab roll-back and trench retreat with respect to the overriding plate. In the mantle wedge, the retreating subduction zone is accompanied by active upwelling of hot asthenospheric material, which replaces the lithospheric mantle of the overriding plate and decouples it from the subducting slab, creating favourable P-T conditions for boninite to adakite magmatism (Fig. 7a). As a geometric consequence of oblique subduction, the simultaneous effect
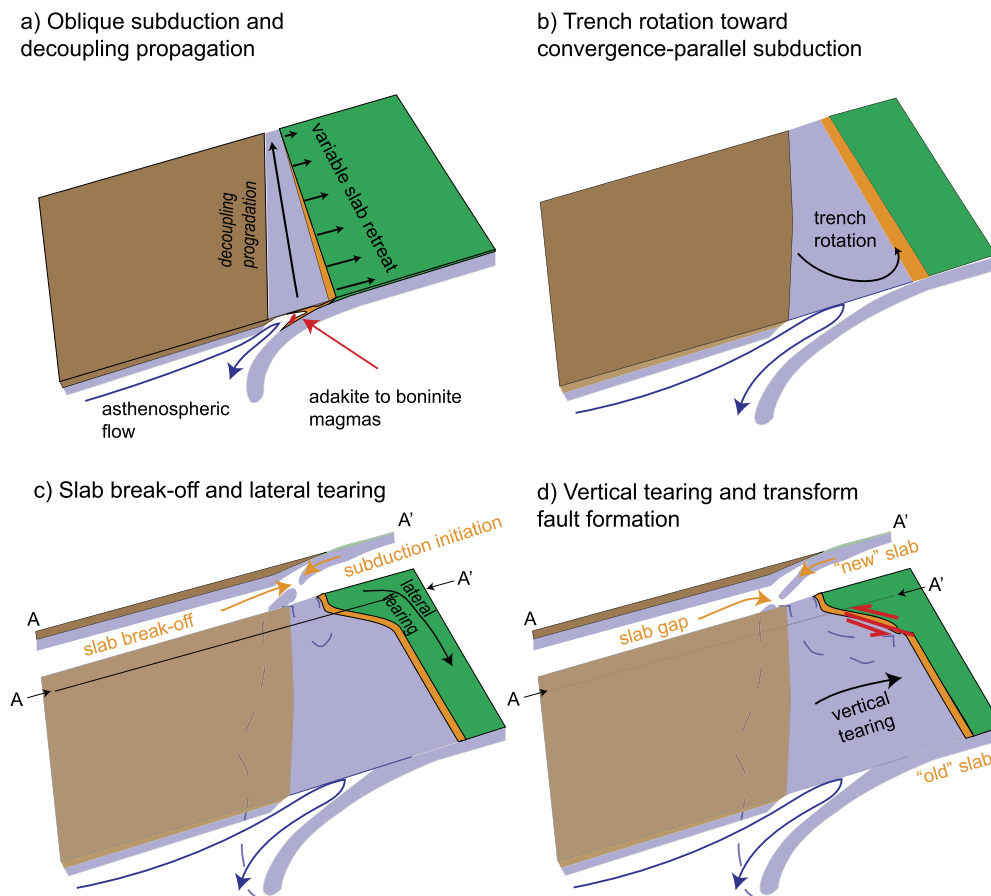
Fig. 7. Conceptual model of slab tearing in a non-collisional environment: a) oblique subduction leading to differential rates of slab retreat along the trench, and the associated propagation of decoupling between overriding and downgoing plates; b) further rotation of the trench, which ended in convergence-parallel subduction; c) initial detachment of the slab, followed by its lateral tearing and bending of the trench; d) transition from horizontal to vertical tearing, and formation of a transform fault between different segments of the subduction zone.

of a trench-normal and a trench-parallel convergence component leads to asymmetric mantle return flow (Balázs et al., 2021) and momentum force (Lallemand et al., 2008; Li and Gurnis, 2023), which in turn promote variable slab retreat velocities along the trench. Decoupling between overriding and downgoing plates (induced by the ascent of the asthenosphere in the mantle wedge) propagates laterally along the active margin. It follows the gradual rotation of the trench and the associated decrease in subduction obliquity, ending in the establishment of convergence-parallel subduction (Fig. 7b). According to the previous studies, along-trench variations in slab retreat rates may also be enhanced by a lateral decrease in the strength of the subduction interface (Balázs et al., 2021) caused by tectonically induced horizontal sediment transport in the accretionary wedge (Malatesta et al., 2013, 2016).

In most of the model results, the overriding and subducting plates begin to decouple ∼6-7 Myr after the start of the simulation (Fig. 6a). Compared to this time, the onset of decoupling is delayed by ∼2-3 Myr in only two cases: (1) for the oldest (90 Ma) subducting slab, whose rigidity requires more time for trench retreat to begin, and (2) for the oceanic overriding plate, whose stronger mantle prevents its rapid replacement by asthenospheric material. The rate of decoupling migration along the trench typically varies between 60 and 100 cm yr^{-1}, increasing to ∼120 cm yr^{-1} in the case of the oldest (90 Ma) subducting plate. Moreover, at a low subduction obliquity angle (7.5°), decoupling propagates even faster (∼150 cm yr^{-1}), while occurring uniformly along the entire length of the active margin (migration rate → ∞) with no initial oblique component (see Fig. 6a).

The obliquity of the active margin promotes the along-trench variation of the dynamic pressure (Balázs et al., 2021). This pressure, when under a certain combination of initial and boundary conditions, can trigger slab break-off and its subsequent lateral propagation (tearing) against the direction of the preceding migration of decoupling between overriding and subducting plates (Fig. 7c). However, in the absence of subduction obliquity and with subducting plates older than 50 Ma, slab break-off does not occur (Fig. 6b). With a relatively small increase in subduction obliquity to 7.5° and a decrease in slab age to 40-50 Ma, detachment of the subducting plate occurs either uniformly or at a high tearing rate (∼150 cm yr^{-1}) along the trench. The youngest slabs (20 Ma and 30 Ma), combined with a reference obliquity of 15°, provide the optimal settings for the lowest tearing velocities of 10-15 cm yr^{-1}, which are comparable to estimates from previous modelling studies (e.g., Burkett and Billen, 2010). Importantly, further increasing the subduction obliquity to 22.5° or changing to an equal partitioning of the boundary velocities (between the subduction component and the advance of the overriding plate) leads to an increase in the rate of tearing to 65 cm yr^{-1}, while break-off becomes quasi-instant (tearing rate → ∞) in the experiment without a subduction component in the total shortening (see Fig. 6b).

The geodynamic regime of an active margin (stable, advancing, or retreating subduction) is known to be mainly controlled by rheological weakening by fluids and melts (Gerya and Meilick, 2011; Baitsch-Ghirardello et al., 2014). In our study, the slab retreat mode is imposed by the rheological model, which includes the combined effect of brittle softening caused by accumulated strain (Huismans and Beaumont, 2002) and ductile damage due to
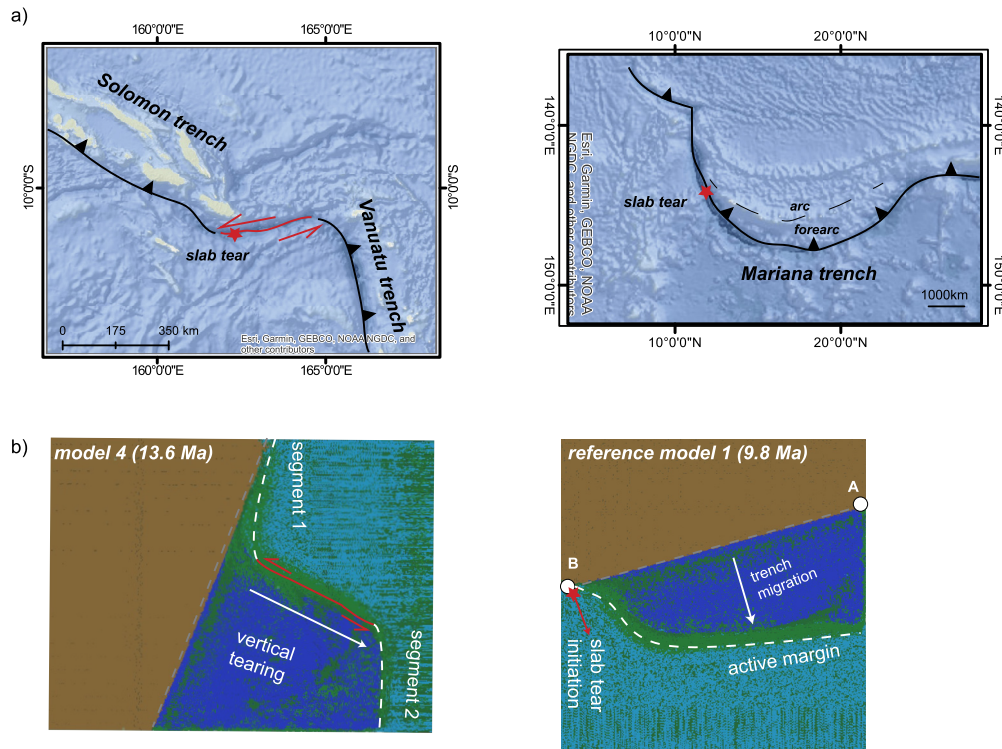
Fig. 8. Comparison of the configuration and structuring of non-collisional plate margins in natural and modelled cases: a) the Solomon and Vanuatu segments of the New Hebrides subduction zone connected by the San Cristobal fault (e.g., Neely and Furlong, 2018) and the Mariana's subduction zone. The red star indicates the connection between lateral and vertical tearing of the downgoing plate (Miller et al., 2006; Zhang et al., 2019); b) plan view of model **4** (obliquity angle of 22.5°) and model **1** (obliquity angle of 15°). Lateral and vertical tearing of the slab is reflected first in trench bending (as in the case of the Marianas) and then in segmentation of the subduction zone by a newly formed transform fault (as in the case of the New Hebrides).

a reduction in grain size (Gerya et al., 2021; Ruh et al., 2022). An additional experiment (Fig. S12), excluding brittle-ductile weakening, shows neither slab tearing norrotation of the trench. In agreement with previous studies (Gerya and Meilick, 2011; Baitsch-Ghirardello et al., 2014; Gerya et al., 2021), this confirms that rheological weakening mechanisms are crucial in the processes of decoupling between overriding and subducting plates and subsequent slab break-off.

Incipient slab break-off is immediately followed by initiation of new subduction as the oceanic plate is pushed further toward the continent by the applied boundary velocities (Fig. 7c). However, the length of this "new" slab (and the associated slab pull force) is much less than in the adjacent segment where the "old" slab has not yet been detached. This sharp contrast between slab pull forces leads to extremely different rates of trench retreat, which in turn result in a strong curvature of the subduction zone. In the final phase, lateral tearing changes direction to vertical and develops into a transform fault along the former curved section of the trench (Fig. 7d). Importantly, this transition from horizontal to vertical tearing occurs only when the propagation of the initial slab break-off is relatively slow (< 70 cm yr^{-1}), as observed only in the experiments with the young slabs (20-30 Myr) and highly oblique margins (15-22.5°), and when the subduction component dominates in the applied convergence (Fig. 6b).

4.2. Comparison of model results to natural examples

In our experiments, the near-trench surface topography responds to the progressive decoupling between the overriding and subducting plate with a gradual shallowing and widening of the basin above the thinned fore-arc and back-arc lithosphere (Fig. 3), which is underlain by the uplifted asthenosphere (Fig. 2). This model outcome is consistent with the observed lateral variations

in the width of Marianas fore-arc reaching up to 200 km (Stern et al., 2004; Gvirtzman and Stern, 2004). A similar process of fore-arc shallowing and widening has been observed in several other subduction systems – such as the Great Valley fore-arc in the Cascadia subduction system (Unruh et al., 2007; Mitchell et al., 2010) and the Talara Basin in the Andean subduction zone (Hessler and Sharman, 2018) – where it has previously been interpreted as the result of subduction of an oceanic plateau or ridge, or preceding phase of shallow subduction.

Uplift of the asthenospheric material creates favourable P-T conditions for partial melting in the shallowest mantle wedge (Fig. 2d; Fig. S1). Similar conditions (P = 0.5-0.9 GPa and T= 1217-1262 °C) are assumed for the generation of adakitic and boninitic lavas in the Marianas fore-arc (Ribeiro et al., 2013). In our results, the obliquity of subduction leads to a progressive migration of decoupling front, predicting younging of magmatism along the fore-arc and thus may provide an explanation for the younging trend observed in ultrapotassic rocks emplaced along the fore-arc of the Late Cretaceous Tethyan margin in the Balkan Peninsula (Sokol et al., 2020). Importantly, the modelled heat flow, which increases from ∼60 mW/m² up to ∼140 mW/m² by the rise of the asthenosphere in the mantle wedge, is consistent with the range of heat flow measurements in the Marianas (∼85-125 mW/m²; Watanabe et al., 1977).

The modelled process of slab break-off is accompanied by toroidal-like deformation in the crust (Fig. 4c1). Recent geodetic observations have revealed similar imprints of the tearing processes around the Calabrian (Palano et al., 2017) and Hellenic (Pérouse et al., 2012) slab edges. The relatively low velocities of slab tearing (10-15 cm yr^{-1}) reproduced in experiments with the youngest (20-30 Ma) slabs (Fig. 6b) are compatible with the rate of tear propagation (∼100 km Myr^{-1}) inferred from the lateral younging trend (∼11.0-3.5 Ma along 900 km) observed in mafic

magmatic products in the Mexico subduction zone (Ferrari et al., 2012).

Horizontal tearing of the slab promotes a curved trench geometry (Fig. 2f), which evolves into a transform fault and leads to segmentation of the subduction zone (Fig. 2g). Such an arcuate trench configuration and segmented subduction boundary over length scales of up to 1500 km are characteristic of several active margins (Fig. 8) such as the New Hebrides (Solomon-Vanuatu trench; Neely and Furlong, 2018), Izu-Bonin-Marianas (e.g., Stern et al., 2004), Tonga (e.g., Garcia-Castellanos et al., 2000), Calabrian (e.g., Faccenna et al., 2007) subduction zones, and the Alpine-Carpathian and Alboran regions (e.g., Wortel and Spakman, 2000).

5. Conclusions

Slab break-off is usually referred to as an early collisional process driven primarily by the slowing of the subduction rate as negatively buoyant oceanic lithosphere detaches from positively buoyant continental lithosphere that is attempting to subduct (e.g., Duretz et al., 2011). In this context, slab tearing (or slab break-off propagation) is traditionally attributed to the dynamics of the continental corner (Fig. 9a), when the subducting plate first detaches in the area of continental collision and then the slab window opens toward the adjacent segment of the convergence boundary where ocean-continent subduction continues (e.g., Li et al., 2013). Another important process, hitherto considered independent of slab break-off and horizontal slab tearing, is a fragmentation of the subducting slab along vertical planes perpendicular to the direction of convergence (Fig. 9b). Previous numerical studies have linked this vertical slab tearing to pre-existing weakness within the subducting plate (Burkett and Billen, 2010) and/or abruptly changing convergence rates along the trench (Cui and Li, 2022).

In our study, we show, for the first time, that horizontal and vertical slab tearing are different stages of the same process, which can develop in a self-sustained manner in a non-collisional setting of continuous subduction (Fig. 9c). Even with an originally absolutely homogeneous oceanic plate and laterally unchanging and temporally constant boundary velocities, the obliquity of the active margin appears to be a sufficient factor to cause a complex system evolution involving various geodynamic processes, each of which has received a significant amount of interest in the literature over the past decade. In addition to horizontal (e.g., Boonma et al., 2021) and vertical slab tearing (e.g., Chen et al., 2022), additional processes active include (see Fig. 7): (1) retreat of the trench (e.g., Gerya and Meilick, 2011), (2) decoupling of the overriding and downgoing plates by upwelling asthenosphere in the mantle wedge (also termed "delamination"; e.g., Ueda et al., 2012), (3) rotation of the trench (e.g., Malatesta et al., 2016), (4) initiation of new subduction (e.g., Stern and Gerya, 2018), and (5) formation of a transform fault (e.g., Özbakır et al., 2020), which may potentially evolve into a Subduction-Transform-Edge-Propagator (STEP) fault (e.g., Govers and Wortel, 2005; Munch et al., 2020). Our results show that all of the aforementioned processes are spatially and temporally coupled and together represent distinct phases in the evolution of the mantle-lithosphere system. Further investigations therefore require the use of modern numerical techniques that can capture the combined effect of mantle flow and lithospheric deformation in a dynamically and rheologically consistent framework.

CRediT authorship contribution statement

All persons who meet authorship criteria are listed as authors, and all authors certify that they have participated sufficiently in the work to take public responsibility for the content, including participation in the concept, design, analysis, writing, or revision
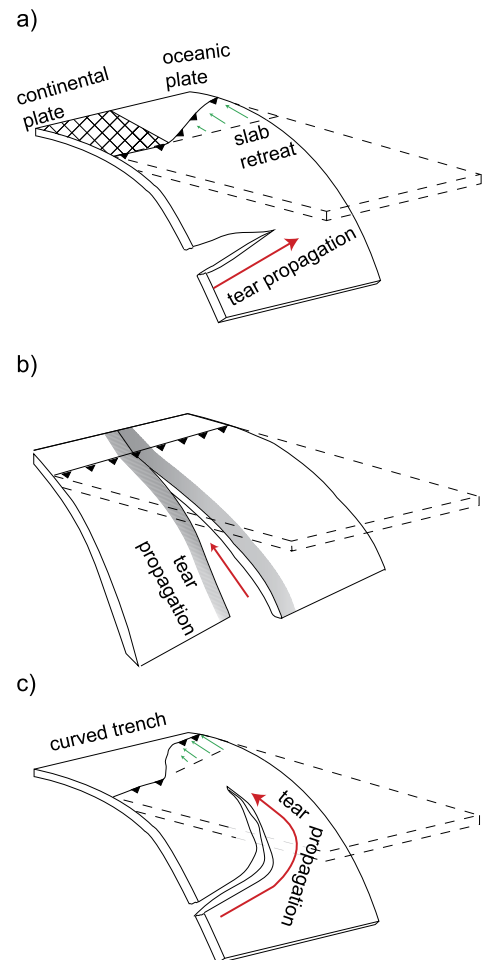
Fig. 9. Three scenarios of tear propagation based on previous (a-b) and our (c) studies: a) horizontal stab tearing associated with a spatial transition between continental collision and oceanic subduction (inspired by Li et al., 2013); b) vertical slab tearing due to a pre-existing zone of weakness in the subducting plate (inspired by Cui and Li, 2022); c) transition from lateral to vertical tearing in the non-collisional setting with oblique subduction of a homogeneous oceanic slab (detected in our experiments).

of the manuscript. Furthermore, each author certifies that this material or similar material has not been and will not be submitted to or published in any other publication before its appearance in the Earth and Planetary Science Letters.

Declaration of competing interest

The authors declare that they have no known competing financial interests or personal relationships that could have appeared to influence the work reported in this paper.

Data availability

Data will be made available on request.

Acknowledgements

Appendix A. Methods

We produced the simulations presented in this contribution using the thermo-mechanical code I3ELVIS (Gerya and Yuen, 2007; Gerya, 2019). This parallel 3D code solves the conservation equations of momentum, mass, and energy by a finite difference method with a marker-in-cell technique. The governing equations, as well as the main equations describing the assumed rheology, are given below.

a) Governing equations

The momentum equations are presented in the form of 3D Stokes flow:

$$
\begin{aligned}
\frac{\partial \sigma'_{xx}}{\partial x} + \frac{\partial \sigma'_{xy}}{\partial y} + \frac{\partial \sigma'_{xz}}{\partial z} &= \frac{\partial P}{\partial x}, \\
\frac{\partial \sigma'_{yx}}{\partial x} + \frac{\partial \sigma'_{yy}}{\partial y} + \frac{\partial \sigma'_{yz}}{\partial z} &= \frac{\partial P}{\partial y} - g\rho, \\
\frac{\partial \sigma'_{zx}}{\partial x} + \frac{\partial \sigma'_{zy}}{\partial y} + \frac{\partial \sigma'_{zz}}{\partial z} &= \frac{\partial P}{\partial z},
\end{aligned}
\tag{A.1}
$$

where x, y, z are coordinates, σ'_{ij} are components of the deviatoric stress tensor, P is pressure, ρ is density depending on composition, pressure, and temperature (see Table A.1), and g is the gravitational acceleration (9.81 m s^{-2}).

The 3D continuity equation describes the conservation of mass for an incompressible medium as follows:

$$
\frac{\partial \vartheta_x}{\partial x} + \frac{\partial \vartheta_y}{\partial y} + \frac{\partial \vartheta_z}{\partial z} = 0,
\tag{A.2}
$$

where ϑ_i are components of the velocity vector.

The mechanical equations are fully thermo-dynamically coupled with the heat conservation equation:

$$
\rho C_p \left(\frac{\partial T}{\partial t} \right) = -\frac{\partial q_x}{\partial x} - \frac{\partial q_y}{\partial y} - \frac{\partial q_z}{\partial z} + H_a + H_s + H_r,
\tag{A.3}
$$

where C_p is effective isobaric heat capacity (incorporating latent heat), T is temperature, t is time, q_i are components of the heat flux vector, H_a is an energetic effect of isothermal (de)compression (i.e. adiabatic heating/cooling), H_s is shear heating, and H_r is radiogenic heat production (see Table A.1).

The heat flux (q_i) is represented by:

$$
\begin{aligned}
q_x &= -\kappa \frac{\partial T}{\partial x}, \\
q_y &= -\kappa \frac{\partial T}{\partial y}, \\
q_z &= -\kappa \frac{\partial T}{\partial z},
\end{aligned}
\tag{A.4}
$$

where κ is temperature- and pressure-depended thermal conductivity (see Table A.1).

The adiabatic (H_a) and shear heating (H_s) components are defined as follows:

$$
H_a = T\alpha \left(\vartheta_x \frac{\partial P}{\partial x} + \vartheta_y \frac{\partial P}{\partial y} + \vartheta_z \frac{\partial P}{\partial z} \right),
\tag{A.5}
$$

$$
H_s = \sigma'_{xx}\dot{\varepsilon}_{xx} + \sigma'_{yy}\dot{\varepsilon}_{yy} + \sigma'_{zz}\dot{\varepsilon}_{zz} + 2\sigma'_{xy}\dot{\varepsilon}_{xy} + 2\sigma'_{yz}\dot{\varepsilon}_{yz} + 2\sigma'_{xz}\dot{\varepsilon}_{xz},
\tag{A.6}
$$

where α is the thermal expansion coefficient and $\dot{\varepsilon}_{ij}$ are components of strain rate tensor:

$$
\dot{\varepsilon}_{ij} = \frac{1}{2} \left(\frac{\partial \vartheta_i}{\partial x_j} + \frac{\partial \vartheta_j}{\partial x_i} \right).
\tag{A.7}
$$

b) Rheology

The deviatoric stress (σ'_{ij}) and strain rate ($\dot{\varepsilon}_{ij}$) are related by a viscous constitutive equation:

$$
\sigma'_{ij} = 2\eta_{eff}\dot{\varepsilon}_{ij},
\tag{A.8}
$$

where η_{eff} is effective viscosity combining the composite contributions of diffusion and dislocation creep with Drucker-Prager plasticity.

For ductile rheology, the contributions of dislocation and diffusion creep are accounted for by the composite viscosity (η_{duct}):

$$
\eta_{duct} = \frac{\eta_{disl}\eta_{diff}}{\eta_{disl} + \eta_{diff}},
\tag{A.9}
$$

where η_{disl} and η_{diff} are effective viscosities for power law dislocation and Newtonian diffusion creep, respectively:

$$
\eta_{disl} = \frac{1}{2} A_{disl}^{\frac{1}{n}} \exp\left(\frac{E_{disl} + PV_{disl}}{nRT} \right) \dot{\varepsilon}_{II}^{\frac{1-n}{n}},
\tag{A.10}
$$

$$
\eta_{diff} = \frac{1}{2} A_{diff} h^m \exp\left(\frac{E_{diff} + PV_{diff}}{RT} \right),
\tag{A.11}
$$

where $A_{disl|diff}$ is a material constant, n is the power law exponent, $E_{disl|diff}$ is the activation energy, $V_{disl|diff}$ is activation volume, R is the gas constant (8.314 J K^{-1} mol^{-1}), $\dot{\varepsilon}_{II} = \sqrt{\frac{1}{2}(\dot{\varepsilon}_{ij})^2}$ is the square root of the second invariant of the strain rate tensor, h is grain size, and m is grain size exponent. For the mantle rocks, the ductile creep model accounts for the processes of grain size reduction and growth assisted by Zener pinning (Bercovici and Ricard, 2012; Mulyukova and Bercovici, 2017).

To yield effective viscous-plastic rheology, the ductile rheology is combined with a brittle (plastic) rheology using the Drucker-Prager criterion:

$$
\eta_{plast} = \frac{1}{2} \frac{C + \mu P}{\dot{\varepsilon}_{II}},
\tag{A.12}
$$

where C is cohesion (rock strength at $P = 0$) and μ is an internal frictional coefficient that depends on the integrated plastic strain $\gamma = \int \sqrt{\frac{1}{2}(\dot{\varepsilon}_{ij(plast)})^2} dt$ as follows:

$$
\mu = \mu_0 - \gamma \mu_\gamma \quad \text{for } \gamma \leq \gamma_0 \quad \text{and} \mu = \mu_1 \quad \text{for } \gamma > \gamma_0,
\tag{A.13}
$$

where μ_0 and μ_1 are initial and final internal friction, and μ_γ is a rate of brittle weakening:

$$
\mu_\gamma = \frac{\mu_0 - \mu_1}{\gamma_0},
\tag{A.14}
$$

where γ_0 is an upper limit for strain-related weakening.

The resulting effective viscosity (η_{eff}) is assigned using a Christmas tree-like criterion, in which the rheological behaviour depends on the minimum between the ductile and brittle/plastic components (Ranalli, 1995; Burov, 2011):

$$
\eta_{eff} = \min\left(\eta_{duct}, \eta_{plast} \right).
\tag{A.15}
$$

The values of the adopted rheological parameters (both ductile and brittle/plastic) can be found in Table A.2.

Table A.1
Density and thermal parameters.

Compositional unit	Reference density, ρ_0 [kg m^{-3}]	Thermal parameters	
		Thermal conductivity, k [W m^{-1} K^{-1}]	Radiogenic heat production, H_r [μW m^{-3}]
Upper continental crust	2750	$0.64+807/(T+77)$	2.0
Lower continental crust	3000	$1.18+474/(T+77)$	0.20
Upper oceanic crust	3000	$1.18+474/(T+77)$	0.22
Lower oceanic crust	3000	$1.18+474/(T+77)$	0.24
Lithospheric mantle	3300	$0.73+1293/(T+77) \exp(4.0 \times 10^{-6}\, P)$	0.022
Sublithospheric mantle	3300	$0.73+1293/(T+77) \exp(4.0 \times 10^{-6}\, P)$	0.024
Weak zone	3300	$0.73+1293/(T+77) \exp(4.0 \times 10^{-6}\, P)$	0.026
References	Bittner and Schmeling (1995); Turcotte and Schubert (2002)	Clauser and Huenges (1995)	Bittner and Schmeling (1995); Turcotte and Schubert (2002)

For the crustal rocks, the heat capacity C_p = 1000 J kg^{-1} K^{-1}, and the density (ρ) is calculated from Boussinesq approximation: $\rho = \rho_0 [1 - \alpha(T - T_0)][1 - \beta(P - P_0)]$, where ρ_0 is the density at normal conditions (T_0 = 298 K; P_0 = 0.1 MPa), $\alpha = 2 \times 10^{-5}$ K^{-1} is thermal expansion, $\beta = 0.6 \times 10^{-5}$ MPa^{-1} is adiabatic compressibility.
For the mantle (including the weak zone), parameters such as density (ρ), thermal expansion (α), adiabatic compressibility (β), and heat capacity (C_p) are computed as a function of pressure (P) and temperature (T) in accordance with the thermodynamic petrology model Perple_X (Connolly, 2005), which includes a number of pressure-induced phase transitions (Ringwood, 1975): from olivine to wadsleyite at ∼410 km depth, wadsleyite to ringwoodite at ∼520 km depth (Katsura and Ito, 1989), and ringwoodite to bridgmanite at ∼660 km depth (Ito et al., 1990).

Table A.2
Rheological parameters.

Compositional unit	Ductile						Brittle/plastic	
	Material constant, $A_{disl|diff}$ [Pa^n s| Pa s]		Power law exponent, n []	Activation energy, $E_{disl|diff}$ [kJ mol^{-1}]	Activation volume, $V_{disl|diff}$ [cm^3 mol^{-1}]	Grain size, h [mm]	Initial internal friction, μ_0 []	Final internal friction, μ_1 []
Upper continental crust	1.97×10^{17}	2.98×10^{11}	2.3	154 154	0 0	-	0.3	0.0
Lower continental crust	4.80×10^{22}	6.79×10^{12}	3.2	238 238	0 0	-	0.3	0.0
Upper oceanic crust	4.80×10^{22}	6.79×10^{12}	3.2	238 238	0 0	-	0.0	0.0
Lower oceanic crust	4.80×10^{22}	6.79×10^{12}	3.2	238 238	0 0	-	0.6	0.2
Lithospheric mantle	9.09×10^{15}	6.67×10^{14}	3.5	530 375	26 7	3.0 (*)	0.6	0.2
Sublithospheric mantle	9.09×10^{15}	6.67×10^{14}	3.5	530 375	26 7	3.0 (*)	0.6	0.2
Weak zone	9.09×10^{15}	6.67×10^{14}	3.5	530 375	26 7	1.0	0.0	0.0
References	Ranalli (1995); Kohlstedt et al. (1995); Burov (2011)						Gerya et al. (2021)	

For all rock types, the cohesion C = 3 MPa, and the upper strain limit for brittle weakening γ_0 = 0.5. In model 12, which excludes the effect of strain-induced weakening in the oceanic crust and mantle, $\mu_1 = \mu_0$.
For the crustal rocks, grain size dependence is included in the material constant A_{diff}. For the mantle rocks, grain size exponent m = 3.0.
(*) In all experiments except model 12, where ductile damage due to grain size reduction is excluded, grain size (h) depends on mechanical work and temperature. See Gerya et al. (2021) for more details.

Appendix B. Supplementary material

Supplementary material related to this article can be found online at https://doi.org/10.1016/j.epsl.2023.118097.

References

Altunkaynak, Ş., Genç, Ş.C., 2008. Petrogenesis and time-progressive evolution of the Cenozoic continental volcanism in the Biga Peninsula, NW Anatolia (Turkey). Lithos 102 (1–2), 316–340.

Andersen, T.B., Jamtveit, B., Dewey, J.F., Swensson, E., 1991. Subduction and eduction of continental crust: major mechanisms during continent-continent collision and orogenic extensional collapse, a model based on the south Norwegian Caledonides. Terra Nova 3 (3), 303–310.

Andrić, N., Vogt, K., Matenco, L., Cvetković, V., Cloetingh, S.A.P.L., Gerya, T., 2018. Variability of orogenic magmatism during Mediterranean-style continental collisions: a numerical modelling approach. Gondwana Res. 56, 119–134.

Artemieva, I.M., 2006. Global 1°×1° thermal model TC1 for the continental lithosphere: implications for lithosphere secular evolution. Tectonophysics 416, 245–277.

Baitsch-Ghirardello, B., Gerya, T.V., Burg, J.P., 2014. Geodynamic regimes of intraoceanic subduction: implications for arc extension vs. shortening processes. Gondwana Res. 25, 546–560.

Balázs, A., Faccenna, C., Ueda, K., Funiciello, F., Boutoux, A., Blanc, E.J.-P., Gerya, T., 2021. Oblique subduction and mantle flow control on upper plate deformation: 3D geodynamic modeling. Earth Planet. Sci. Lett. 569, 117056.

Barazangi, M., Isacks, B.L., Oliver, J., Dubois, J., Pascal, G., 1973. Descent of lithosphere beneath New Hebrides, Tonga-Fiji and New Zealand: evidence for detached slabs. Nature 242 (5393), 98–101.

Baumann, C., Gerya, T.V., Connolly, J.A., 2010. Numerical modelling of spontaneous slab breakoff dynamics during continental collision. Geol. Soc. (Lond.) Spec. Publ. 332 (1), 99–114.

Bercovici, D., Ricard, Y., 2012. Mechanisms for the generation of plate tectonics by two-phase grain-damage and pinning. Phys. Earth Planet. Inter. 202, 27–55.

Bevis, M., et al., 1995. Geodetic observations of very rapid convergence and back-arc extension at the Tonga arc. Nature 374 (6519), 249–251.

Bird, P., 1998. Testing hypotheses on plate-driving mechanisms with global lithosphere models including topography, thermal structure, and faults. J. Geophys. Res., Solid Earth 103 (B5), 10115–10129.

Bittner, D., Schmeling, H., 1995. Numerical modelling of melting processes and induced diapirism in the lower crust. Geophys. J. Int. 123 (1), 59–70.

Boonma, K., García-Castellanos, D., Jiménez-Munt, I., Gerya, T.V., 2021. Thermomechanical modelling of lithospheric slab tearing and its topographic response. Application to the Gibraltar Arc. J. Geophys. Res., Solid Earth. Submitted for publication. https://doi.org/10.1002/essoar.10508757.1.

Buiter, S.J., Govers, R., Wortel, M.J.R., 2002. Two-dimensional simulations of surface deformation caused by slab detachment. Tectonophysics 354 (3–4), 195–210.

Burkett, E.R., Billen, M.I., 2010. Three-dimensionality of slab detachment due to ridge-trench collision: laterally simultaneous boudinage versus tear propagation. Geochem. Geophys. Geosyst. 11 (11), Q11012.

Burov, E., Yamato, P., 2008. Continental plate collision, P–T–t–z conditions and unstable vs. stable plate dynamics: insights from thermo-mechanical modelling. Lithos 103 (1–2), 178–204.

Burov, E.B., 2011. Rheology and strength of the lithosphere. Mar. Pet. Geol. 28 (8), 1402–1443.

Chen, Y., Chen, H., Liu, M., Gerya, T., 2022. Vertical tearing of subducting slabs controlled by geometry and rheology of oceanic plates. https://doi.org/10.21203/rs.3.rs-1688564/v1.

Clauser, C., Huenges, E., 1995. Thermal conductivity of rocks and minerals. In: Ahrens, T. (Ed.), Rock Physics and Phase Relations. A Handbook of Physical Constants. AGU Reference Shelf 3. American Geophysical Union, Washington DC, pp. 105–126.

Connolly, J.A., 2005. Computation of phase equilibria by linear programming: a tool for geodynamic modeling and its application to subduction zone decarbonation. Earth Planet. Sci. Lett. 236 (1–2), 524–541.

Crameri, F., et al., 2012. A comparison of numerical surface topography calculations in geodynamic modelling: an evaluation of the 'sticky air' method. Geophys. J. Int. 189 (1), 38–54.

Cui, Q., Li, Z.H., 2022. Along-strike variation of convergence rate and pre-existing weakness contribute to Indian slab tearing beneath Tibetan Plateau. Geophys. Res. Lett. 49 (4), e2022GL098019.

Curray, J.R., 1989. The Sunda Arc: a model for oblique plate convergence. Neth. J. Sea Res. 24 (2–3), 131–140.

Duretz, T., Gerya, T.V., May, D.A., 2011. Numerical modelling of spontaneous slab breakoff and subsequent topographic response. Tectonophysics 502, 244–256.

Duretz, T., Gerya, T.V., Kaus, B.J.P., Andersen, T.B., 2012b. Thermomechanical modeling of slab eduction. J. Geophys. Res. 117, B08411. https://doi.org/10.1029/2012JB009137.

Duretz, T., Schmalholz, S.M., Gerya, T.V., 2012a. Dynamics of slab detachment. Geochem. Geophys. Geosyst. 13 (3), Q03020.

Duretz, T., Gerya, T.V., Spakman, W., 2014. Slab detachment in laterally varying subduction zones: 3-D numerical modeling. Geophys. Res. Lett. 41, 1951–1956. https://doi.org/10.1002/2014GL059472.

Faccenna, C., Funiciello, F., Civetta, L., D'Antonio, M., Moroni, M., Piromallo, C., 2007. Slab disruption, mantle circulation, and the opening of the Tyrrhenian basins. In: Beccaluva, L., Bianchini, G., Wilson, M. (Eds.), Cenozoic Volcanism in the Mediterranean Area. In: Geol. Soc. Am. Spec. Pap., vol. 418, pp. 153–169.

Ferrari, L., 2004. Slab detachment control on mafic volcanic pulse and mantle heterogeneity in central Mexico. Geology 32 (1), 77–80.

Ferrari, L., Orozco-Esquivel, T., Manea, V., Manea, M., 2012. The dynamic history of the trans-Mexican volcanic belt and the Mexico subduction zone. Tectonophysics 522–523, 122–149. https://doi.org/10.1016/j.tecto.2011.09.018.

Garcia-Castellanos, D., Torne, M., Fernàndez, M., 2000. Slab pull effects from a flexural analysis of the Tonga and Kermadec trenches (Pacific Plate). Geophys. J. Int. 141 (2), 479–484.

Gerya, T., 2011. Future directions in subduction modeling. J. Geodyn. 52 (5), 344–378.

Gerya, T., 2019. Introduction to Numerical Geodynamic Modelling, 2nd edition. Cambridge University Press, p. 471.

Gerya, T., 2022. Numerical modeling of subduction: state of the art and future directions. Geosphere 18 (2), 503–561.

Gerya, T.V., Meilick, F.I., 2011. Geodynamic regimes of subduction under an active margin: effects of rheological weakening by fluids and melts. J. Metamorph. Geol. 29 (1), 7–31.

Gerya, T.V., Yuen, D.A., 2007. Robust characteristics method for modelling multiphase visco-elasto-plastic thermo-mechanical problems. Phys. Earth Planet. Inter. 163 (1–4), 83–105. https://doi.org/10.1016/j.pepi.2007.04.015.

Gerya, T.V., Yuen, D.A., Maresch, W.V., 2004. Thermomechanical modelling of slab detachment. Earth Planet. Sci. Lett. 226 (1–2), 101–116.

Gerya, T.V., Bercovici, D., Becker, T.W., 2021. Dynamic slab segmentation due to brittle–ductile damage in the outer rise. Nature 599, 245–250.

Govers, R., Wortel, M.J.R., 2005. Lithosphere tearing at STEP faults: response to edges of subduction zones. Earth Planet. Sci. Lett. 236 (1–2), 505–523. https://doi.org/10.1016/j.epsl.2005.03.022.

Gvirtzman, Z., Stern, R.J., 2004. Bathymetry of Mariana trench-arc system and formation of the challenger deep as a consequence of weak plate coupling. Tectonics 23. https://doi.org/10.1029/2003TC001581.

Hafkenscheid, E., Wortel, M.J.R., Spakman, W., 2006. Subduction history of the Tethyan region derived from seismic tomography and tectonic reconstructions. J. Geophys. Res., Solid Earth 111 (B8), B08401.

Hessler, A.M., Sharman, G.R., 2018. Subduction zones and their hydrocarbon systems. Geosphere 14 (5), 2044–2067. https://doi.org/10.1130/GES01656.1.

Huismans, R.S., Beaumont, C., 2002. Asymmetric lithospheric extension: the role of frictional plastic strain softening inferred from numerical experiments. Geology 30 (3), 211–214.

Isacks, B., Molnar, P., 1969. Mantle earthquake mechanisms and the sinking of the lithosphere. Nature 223 (5211), 1121–1124.

Ito, E., Akaogi, M., Topor, L., Navrotsky, A., 1990. Negative pressure-temperature slopes for reactions formign MgSiO3 perovskite from calorimetry. Science 249 (4974), 1275–1278.

Katsura, T., Ito, E., 1989. The system Mg2SiO4-Fe2SiO4 at high pressures and temperatures: precise determination of stabilities of olivine, modified spinel, and spinel. J. Geophys. Res., Solid Earth 94 (B11), 15663–15670.

Katz, R.F., Spiegelman, M., Langmuir, C.H., 2003. A new parameterization of hydrous mantle melting. Geochem. Geophys. Geosyst. 4 (9), 1073.

Kohlstedt, D.L., Evans, B., Mackwell, S.J., 1995. Strength of the lithosphere: constraints imposed by laboratory experiments. J. Geophys. Res., Solid Earth 100 (B9), 17587–17602.

Koptev, A., Beniest, A., Gerya, T., Ehlers, T.A., Jolivet, L., Leroy, S., 2019. Plume-induced breakup of a subducting plate: microcontinent formation without cessation of the subduction process. Geophys. Res. Lett. 46 (7), 3663–3675.

Koptev, A.I., Ershov, A.V., 2011. Thermal thickness of the Earth's lithosphere: a numerical model. Moscow Univ. Geol. Bull. 66 (5), 323–330. https://doi.org/10.3103/s014587521105005x.

Lallemand, S., Heuret, A., Faccenna, C., Funiciello, F., 2008. Subduction dynamics as revealed by trench migration. Tectonics 27 (3). https://doi.org/10.1029/2007TC002212.

Li, Y., Gurnis, M., 2023. A simple force balance model of subduction initiation. Geophys. J. Int. 232 (1), 128–146. https://doi.org/10.1093/gji/ggac332.

Li, Z.H., Xu, Z., Gerya, T., Burg, J.P., 2013. Collision of continental corner from 3-D numerical modeling. Earth Planet. Sci. Lett. 380, 98–111.

Malatesta, C., Gerya, T., Crispini, L., Federico, L., Capponi, G., 2013. Oblique subduction modelling indicates along-trench tectonic transport of sediments. Nat. Commun. 4 (1), 1–6.

Malatesta, C., Gerya, T., Crispini, L., Federico, L., Capponi, G., 2016. Interplate deformation at early-stage oblique subduction: 3-D thermomechanical numerical modeling. Tectonics 35 (7), 1610–1625.

Martin, A.K., 2014. Concave slab out board of the Tonga subduction zone caused by opposite toroidal flows under the North Fiji Basin. Tectonophysics 622, 56–61.

Menant, A., Sternai, P., Jolivet, L., Guillou-Frottier, L., Gerya, T., 2016. 3D numerical modeling of mantle flow, crustal dynamics and magma genesis associated with slab roll-back and tearing: the eastern Mediterranean case. Earth Planet. Sci. Lett. 442, 93–107.

Meulenkamp, J.E., Kováč, M., Cicha, I., 1996. On Late Oligocene to Pliocene depocentre migrations and the evolution of the Carpathian-Pannonian system. Tectonophysics 266 (1–4), 301–317. https://doi.org/10.1016/S0040-1951(96)00195-3.

Miller, M.S., Kennett, B.L.N., Toy, V.G., 2006. Spatial and temporal evolution of the subducting Pacific plate structure along the western Pacific margin. J. Geophys. Res. 111, B02401. https://doi.org/10.1029/2005JB003705.

Mitchell, C., Graham, S.A., Suek, D.H., 2010. Subduction complex uplift and exhumation and its influence on Maastrichtian forearc stratigraphy in the Great Valley Basin, northern San Joaquin Valley, California. Geol. Soc. Am. Bull. 122 (11–12), 2063–2078. https://doi.org/10.1130/B30180.1.

Mulyukova, E., Bercovici, D., 2017. Formation of lithospheric shear zones: effect of temperature on two-phase grain damage. Phys. Earth Planet. Inter. 270, 195–212.

Munch, J., Gerya, T., Ueda, K., 2020. Oceanic crust recycling controlled by weakening at slab edges. Nat. Commun. 11, 2009.

Neely, J.S., Furlong, K.P., 2018. Evidence of displacement-driven maturation along the San Cristobal Trough transform plate boundary. Earth Planet. Sci. Lett. 485, 88–98.

Özbakır, A.D., Govers, R., Fichtner, A., 2020. The Kefalonia Transform Fault: a STEP fault in the making. Tectonophysics 787, 228471.

Palano, M., Piromallo, C., Chiarabba, C., 2017. Surface imprint of toroidal flow at retreating slab edges: the first geodetic evidence in the Calabrian subduction system. Geophys. Res. Lett. 44, 845–853. https://doi.org/10.1002/2016GL071452.

Pérouse, E., Chamot-Rooke, N., Rabaute, A., Briole, P., Jouanne, F., Georgiev, I., Dimitrov, D., 2012. Bridging onshore and offshore presentday kinematics of central and eastern Mediterranean: implications for crustal dynamics and mantle flow. Geochem. Geophys. Geosyst. 13, Q09013. https://doi.org/10.1029/2012GC004289.

Ranalli, G., 1995. Rheology of the Earth, 2nd edition. Chapman and Hall, p. 413.

Ribeiro, J.M., Stern, R.J., Martinez, F., Ishizuka, O., Merle, S.G., Kelley, K., Anthony, E.Y., Ren, M., Ohara, Y., Reagan, M., Girard, G., Bloomer, S.H., 2013. Geodynamic evolution of a forearc rift in the southernmost Mariana Arc. Isl. Arc 22 (4), 453–476. https://doi.org/10.1111/iar.12039.

Ringwood, A.E., 1975. Composition and Petrology of the Earth's Mantle. MacGraw-Hill, p. 618.

Rogers, R., Karason, H., van der Hilst, R., 2002. Epeirogenic uplift above a detached slab in northern Central America. Geology 30, 1031–1034.

Ruh, J.B., Tokle, L., Behr, W.M., 2022. Grain size evolution controls on lithospheric weakening during continental rifting. Nat. Geosci. 15, 285–590.

Sokol, K., Prelević, D., Romer, R.L., Božović, M., van den Bogaard, P., Stefanova, E., Kostić, B., Čokulov, N., 2020. Cretaceous ultrapotassic magmatism from the Sava-Vardar Zone of the Balkans. Lithos 354–355, 105268.

Spakman, W., 1990. Tomographic images of the upper mantle below central Europe and the Mediterranean. Terra Nova 2 (6), 542–553.

Stern, R.J., Gerya, T., 2018. Subduction initiation in nature and models: a review. Tectonophysics 746, 173–198.

Stern, R.J., Fouch, M.J., Klemperer, S.L., 2004. An overview of the Izu-Bonin-Mariana subduction factory. In: Eiler, J. (Ed.), Inside the Subduction Factory.

Sternai, P., Jolivet, L., Menant, A., Gerya, T., 2014. Driving the upper plate surface deformation by slab rollback and mantle flow. Earth Planet. Sci. Lett. 405, 110–118.

Turcotte, D.L., Schubert, G., 2002. Geodynamics. Cambridge University Press, p. 456.

Ueda, K., Gerya, T.V., Burg, J.P., 2012. Delamination in collisional orogens: thermo-mechanical modeling. J. Geophys. Res., Solid Earth 117 (B8), B08202.

Unruh, J.R., Dumitru, T.A., Sawyer, T.L., 2007. Coupling of Early Tertiary Extension in the Great Valley Forearc Basin with Blueschist Exhumation in the Underlying Franciscan Accretionary Wedge at Mount Diablo, vol. 119. Geological Society of America Bulletin, California, pp. 1347–1367.

Van de Zedde, D.M.A., Wortel, M.J.R., 2001. Shallow slab detachment as a transient source of heat at midlithospheric depths. Tectonics 20 (6), 868–882.

Van der Meulen, M.J., Kouwenhoven, T.J., Van der Zwaan, G.J., Meulenkamp, J.E., Wortel, M.J.R., 1999. Late Miocene uplift in the Romagnan Apennines and the detachment of subducted lithosphere. Tectonophysics 315 (1–4), 319–335.

Van Hunen, J., Allen, M.B., 2011. Continental collision and slab break-off: a comparison of 3-D numerical models with observations. Earth Planet. Sci. Lett. 302, 27–37.

Watanabe, T., Langseth, M.G., Anderson, R.N., 1977. Heat flow in back-arc basins of the Western Pacific. In: Talwani, M., Pitman III, W.C. (Eds.), Island Arcs Deep Sea Trenches and Back-Arc Basins. American Geophysical Union, Washington, D.C., pp. 137–162.

Widiyantoro, S., van der Hilst, R., 1996. Structure and evolution of lithospheric slab beneath the Sunda arc, Indonesia. Science 271 (5255), 1566–1570.

Wortel, M.J.R., Spakman, W., 1992. Structure and dynamics of subducted lithosphere in the Mediterranean region. Proc. K. Ned. Akad. Wet. 95 (3), 325–347.

Wortel, M.J.R., Spakman, W., 2000. Geophysics – subduction and slab detachment in the Mediterranean-Carpathian region. Science 290 (5498), 1910–1917.

Zhang, H., Wang, F., Myhill, R., et al., 2019. Slab morphology and deformation beneath Izu-Bonin. Nat. Commun. 10, 1310. https://doi.org/10.1038/s41467-019-09279-7.